

Temperature-Driven Strategy for Engineering of Al-Doped ZnO Mesocrystals' Hierarchical Architecture

*Guohui Yang**, *Marcel Kévin Jiokeng Dongmo*, *Simon Buchheiser*, *Thomas Meurer*, *Hermann Nirschl*

G. Yang, S. Buchheiser, H. Nirschl

Institute of Mechanical Process Engineering and Mechanics

Process Machines Group

Karlsruhe Institute of Technology, Strasse am Forum 7, 76131, Germany

E-mail: guohui.yang@kit.edu

M. K. J. Dongmo, T. Meurer

Institute of Mechanical Process Engineering and Mechanics

Digital Process Engineering Group

Karlsruhe Institute of Technology, Hertzstr. 16, 76187, Germany

Keywords: Al-doped ZnO (AZO) mesocrystals, sol-gel synthesis, hierarchical nanostructure characterization, X-ray scattering, dynamic light scattering

Abstract

Nanomaterial functionality is influenced by particle size, morphology and composition. This study introduces a novel temperature-controlled sol-gel method to tailor hierarchical nanostructures, utilizing Al-doped ZnO (AZO) nanoparticles as a case study. AZOs' electrical and optical properties are critical for photovoltaics applications, where controlling crystal properties to optimize conductivity and transparency is key. AZO nanoparticles were synthesized from zinc acetylacetonate hydrate, aluminum isopropoxide and benzylamine in a closed batch reactor. By adjusting temperature profiles — controlling synthesis temperature and heating duration, the method modifies AZO's hierarchical structure. Characterization via electron microscopy, X-ray scattering, and dynamic light scattering, reveals that minor temperature variations (105 °C to 125 °C) affect particle morphologies, exhibiting tunable size, ranging from 18 nm to 41 nm, with higher temperatures promoting aggregation despite existing structure shrinkage. This highlights strong dependency of nucleation and structural formation on temperature profiles, offering a versatile method for tuning nanomaterials for advanced applications.

1. Introduction

In the context of energy transition and the current shortage of rare earth semiconductors, developing alternative methods for incorporating functional nanomaterials into complex optoelectronic semiconductor systems, such as organic light-emitting diodes and thin-film solar cells, is of significant scientific importance [1-4]. Crucially, controlling the size, morphology and dopant level of these materials is essential for their performance [5,6]. Within this domain, wurtzite ZnO, a wide-band-gap semiconductor, has garnered substantial attention for its diverse applications in sensors, solar cells, and transparent conducting films [7,8]. Particularly noteworthy is AZO, valued for its tunable bandgap [8-10], and low electrical resistivity in thin films [11-13], making it as an economically and environmentally viable alternative to rare earth semiconductors, e.g., indium tin oxides and GaN [2-4,14-17]. However, the precision engineering of AZO's characteristics, crucial for tailoring its optical and electrical properties, necessitates a comprehensive understanding of particle-related attributes, such as size and morphology throughout the fabrication process.

The non-aqueous sol-gel process has emerged as a promising technique to produce crystalline metal oxides with controlled particle characteristics through selection of solvents and precursors [18-23]. Despite various synthesis routes, a fundamental understanding of how

reaction parameters influence particle properties remains incomplete. Prior research has shown that factors such as pH and precursor concentration significantly affect the morphology of metal oxide nanoparticles [6,22-29]. Variations in H^+ or OH^- concentrations influence metal-oxygen bond polymerization during ZnO growth [30], while changes in sol concentration affect particle size through colloidal particle interactions [25,26,31]. However, adjusting concentration as a strategy for tuning particle properties has practical limitations, including increased costs, heat transfer inefficiencies, and potential for native point defects at high concentrations [25], as well as poor crystallinity at low concentrations [26,27]. Temperature is another key parameter that significantly affects particle characteristics. Although studies on nanoparticles, e.g., TiO_2 and ZnO, have shown that increasing reaction temperature accelerates reactions and affects particle size and morphology [31,32], a systematic analysis of how both synthesis temperature and heating duration to reach the synthesis temperature influence hierarchical nanoparticle properties is still missing. Understanding the impact of these factors on particle nucleation, size, and aggregation is crucial for precisely tailoring nanomaterials to specific applications.

In this work, a pioneering temperature-controlled sol-gel method is introduced to fine-tune the hierarchical structure of nanocrystals, specifically AZOs. This strategy considers the combined effects of synthesis temperature and heating duration through precisely controlled temperature profiles. The precursor, zinc acetylacetonate hydrate, and doping agent, aluminum isopropoxide, are dispersed in benzylamine at 50 °C, followed by controlled temperature profiles to modulate nucleation. The hierarchical structures of the resulting AZO mesocrystals (Figure 1 a-b) have been evaluated using multiple methodologies, to assess size, morphology, composition and aggregation behavior: 1) Small angle X-ray scattering (SAXS) to quantify the hierarchical sizes of AZO; 2) Dynamic light scattering (DLS) to determine the Z-average (\bar{Z}), polydispersity index (PDI), and size distributions (PSD) of mesocrystals, as well as aggregates of mesocrystals after stabilization with 2-(2-methoxyethoxy)ethoxy)acetic acid (MEAA); 3) Energy-dispersive X-ray spectroscopy (EDX) and image analysis facilitated by transmission electron microscopy (TEM), scanning electron microscopy (SEM), and high-angle annular dark-field imaging (HAADF-STEM) provided insights into the composition and morphology of AZOs; 4) Gravimetric analysis, combined with SAXS data, allowed for the determination of the hierarchical crystal number, including nuclei, primary particles, and mesocrystals, thereby quantifying the effect of temperature profiles on nucleation.

Characterization of AZO products synthesized under different temperature profiles (Figure 1c: heating stage from 50 °C to various synthesis temperatures over defined durations) reveals the substantial influence of both synthesis temperature and heating duration on nucleation and structural evolution. Figure 1a indicates higher synthesis temperatures above 50 °C promoting the formation of primary AZO crystals, which subsequently assemble into mesocrystals. As the temperature increases, the mesocrystal size decreases, but beyond a certain threshold, further temperature elevation leads to mesocrystal aggregation and irregular size amplification. Heating duration (Figure 1b) also plays a crucial role in influencing nucleation mechanisms, impacting particle size and morphology. This study demonstrates the effectiveness of the temperature-controlled sol-gel method in tailoring nanoparticles, particularly AZO mesocrystals by simultaneously controlling synthesis temperature and heating duration, providing valuable insights for optimizing functional nanomaterials for diverse applications.

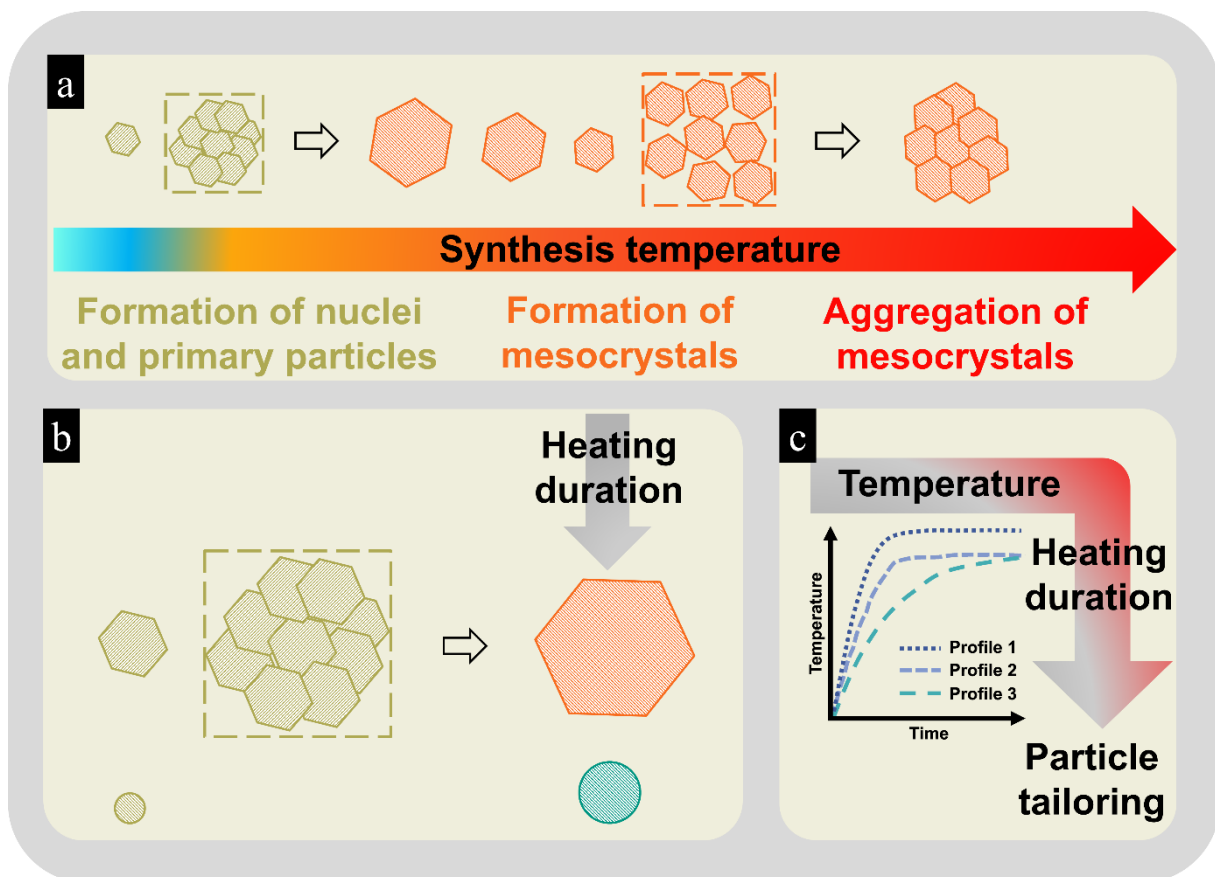


Figure 1. Schematic illustration of the temperature-controlled approach for AZO synthesis: a) impact of synthesis temperatures on AZO's hierarchical structures; b) influence of heating durations on nucleation mechanisms; c) exemplary temperature profiles for particle tailoring.

2. Materials and methods

Chemicals and solvents were supplied from either Sigma–Aldrich unless otherwise mentioned. 2-(2-methoxyethoxy)ethoxy)acetic acid (MEAA) was diluted with ethanol for the stabilization step to facilitate the precision of Eppendorf pipettes when transferring the acid into samples. All other chemicals were used as received. The employed materials and laboratory equipment are described in the following sections.

2.1. Non-aqueous sol-gel synthesis

Pinna and coworkers pioneered the utilization of metal acetylacetonates as precursors, employing benzylamine as a reactive solvent to facilitate metal oxide formation [33]. In this study, 25 g L⁻¹ crystalline reagents (97.5 mol% zinc acetylacetonate hydrate, 2.5 mol% aluminum isopropoxide) and 250 ml aromatic solvent benzylamine were introduced into a closed batch reactor to synthesize AZO particles. The synthesis was initially prepared by heating Zn(acac)₂ and Al(OiPr)₃ in BnNH₂ up to 50 °C. The rotational speed of the magnetic rotor was constant at 850 rpm. Continuous stirring at 50 °C for 60 minutes was conducted to minimize clump formation and no reaction kinetics was observed during this period (Figure S1). Subsequent heating stage began from 50°C, marking the onset of sampling time. Over a specified heating duration, the reactor temperature was further raised to the defined synthesis temperature, thereby initiating nucleation. Figure 2 depicts the pathway of a combined solvolysis-condensation mechanism, leading to the formation of zinc hydroxyl compounds. A subsequent condensation step results in the formation of Zn-O-Zn bonds that are monomeric species to initiate nucleation [34,35]. Additionally, by introducing 2.5 mol% aluminum isopropoxide (Al(OiPr)₃), exclusively as Al³⁺ donor for doping, AZO particles were synthesized.

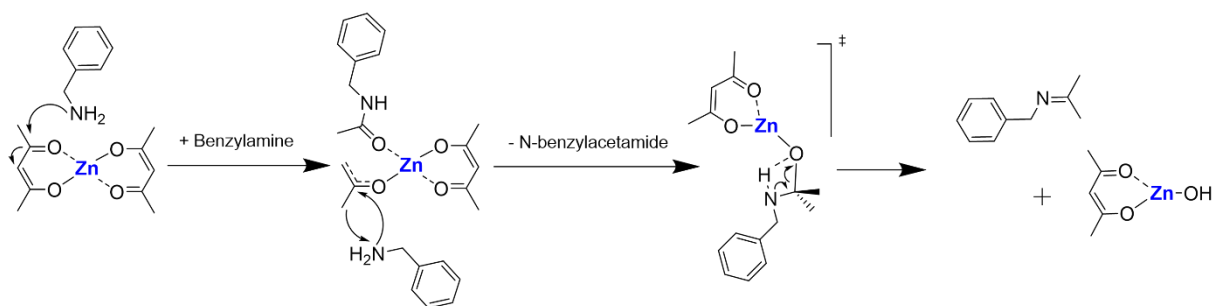


Figure 2. Pathway of a combined solvolysis-condensation mechanism resulting in the formation of zinc hydroxyl compounds with Zn–OH bonds. A following condensation step converts Zn–OH groups into monomeric Zn–O–Zn bonds.

2.2. Closed batch reactor

The closed batch reactor depicted in Figure 3 has a maximum reactor volume of 300 ml and is made of stainless steel. A rising tube with a needle valve for sample extraction is attached to the lid of the reactor. The necessary regulation of the overpressure for sample extraction is achieved through the valve of the compressed air line. Additionally, two heating cartridges pass through the lid into the reactor interior, which are controlled by a PI controller via an E-box and LabVIEW. Pressure and temperature measurements in the reactor are carried out by a pressure sensor onto the lid and a thermometer into the reactor. LabVIEW handles the collected measurement data and the regulation of the magnetic stirrer motor speed. The process control technology is housed in an E-box behind the reactor. In the E-box, components for measurements and regulation of the operating parameters are correlated. To ensure high performance of mixing, the precursor and the doping agent are stirred with the benzylamine by a triangular stirring bar (NeoLab), with the corresponding magnetic stirrer motor mounted directly below the reactor bottom. The reactor can be securely sealed by tightening screws and a sealing ring between the lid and the reactor vessel to ensure a closed system.

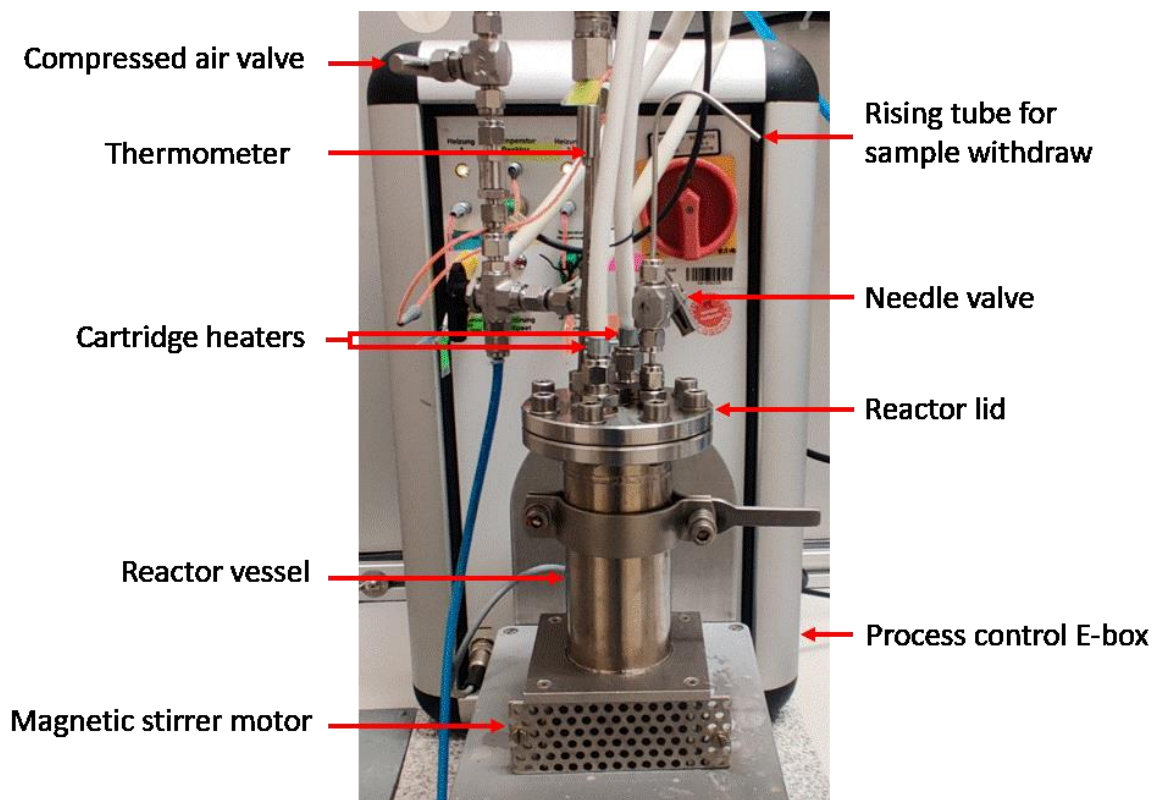


Figure 3. Closed batch reactor and its fundamental elements, including a compressed air valve, a thermometer, two heating cartridges, the reactor vessel and lid, a magnetic stirrer motor, a rising tube with a needle valve for sample extraction, and an E-box.

2.3. Regulation of reactor temperatures

When designing the temperature profiles, following requirements were considered: a) attainment of synthesis temperature with negligible overshoot, b) minimized fluctuations in reactor temperature, and c) reproducible profiles in exponential shape. To meet these criteria, a proportional-integral (PI) controller was implemented in LabVIEW based on the reactor temperature model, designed by utilizing a first-order lag system, typically referred to as a PT1 element in control systems engineering [36]. This setup allowed for the realization of various exponential profiles by defining the synthesis temperature T_r as a constant setpoint and adjusting the time constant τ , within the range from 50 °C to the synthesis temperature. The reactor temperature model is defined by a first-order ordinary differential equation (see Equation 1) for control purposes [37] and the solution is presented in Equation 2. This model was also used to design a moving horizon estimator of the underlying particulate system [38].

$$\tau \frac{d}{dt} T(t) = -T(t) + T_r, \quad t > 0, \quad \text{where } T(t_0) = T_0 \quad (1)$$

$$T(t) = T_{50} e^{-\frac{t-t_0}{\tau}} + T_r \left(1 - e^{-\frac{t-t_0}{\tau}}\right), \quad \text{for } t \geq t_0 \text{ and } T_{50} = T(t_0) \quad (2)$$

Here, different temperature profiles were obtained for various τ and $T_r \in \{105, 110, 125\}$ °C. The time constant τ illustrates how quickly the system responds due to its dynamics or inertia. Systems with a large time constant τ require more time to reach the final value, whereas systems with a small time constant τ reach the initial value more quickly. As a result, the temperature trajectory $T(t)$ in Equation 1 initially rises exponentially and then approaches a limit T_r . The signal theoretically requires 5τ to reach 99.2% of the setpoint. Figure 4 presents all the employed temperature profiles in this publication. The syntheses A – D, T105 as well as T125 were performed by implementing the temperature-control setup, achieving exponential temperature profiles. It is noted that for the whole heating process starting from the room temperature to the synthesis temperature, τ_1 and τ_2 are defined. On one hand, for the first heating phase (25°C → 50°C), $\tau_1 = 90$ s for all the syntheses. It took approximately 7 minutes to reach 50°C, where the residence time at 50°C was 60 minutes, to improve the dispersion of precursors into benzylamine. On the other hand, for the second heating phase from 50 °C ($T_{50} \rightarrow T_r$), τ_2 is defined which varies in individual synthesis and thus receives more attention. τ_2 was manipulated to change the heating time from 50°C to individual synthesis temperature. To summarize, given a defined synthesis temperature T_r and values of τ , a customized profile can be generated in a reproducible manner. For syntheses in this publication, due to the constant τ_1 and resulting similarity in the first heating phase, only the second heating phase from 50 °C is

depicted in Figure 4 and the corresponding theoretical time constant τ_2 for each synthesis is listed in Table 1.

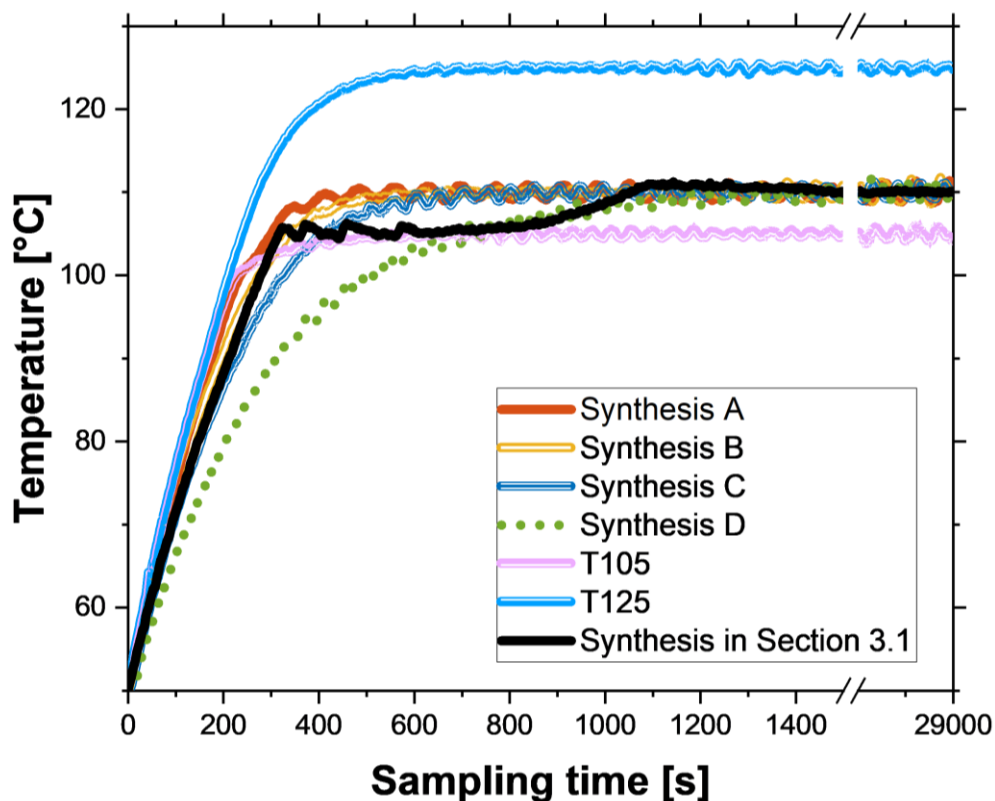


Figure 4. Employed temperature profiles for synthesis in the publication.

Table 1. Synthesis temperature, theoretical time constant of PT1 element for the second heating stage from 50°C to reach the synthesis temperature and heating duration.

Synthesis	Synthesis temperature T_r	τ_2	Heating duration
	[°C]		
A	110	90	7
B	110	120	9
C	110	150	12
D	110	230	19
T105	105	100	8
T125	125	120	10

2.4. Workflow of postprocessing and measurement techniques

Figure 5 presents the workflow of postprocessing after syntheses, to purify and characterize AZO particles. The preparation of AZO particles was ensured through multiple wash steps with ethanol and centrifugation up to 8 hours with a g-force of 7200 at 20°C (Centrifuge 5430R,

rotor F35630, Eppendorf) to eliminate byproducts and remaining reactants [39]. The purified AZO nanocrystals present in ethanol were characterized via several techniques: 1) small angle X-ray scattering (XEUSS 2.0, XENOCs) to determine the geometric mean diameters of primary and mesocrystals, 2) dynamic light scattering via Zetasizer (Nano ZS, Malvern) after the stabilization step to measure the PSD of the stabilized phase, 3) EDX and image analysis, including scanning electron microscopy, transmission electron microscopy and high-angle annular dark-field imaging, 4) drying for gravimetric analysis.

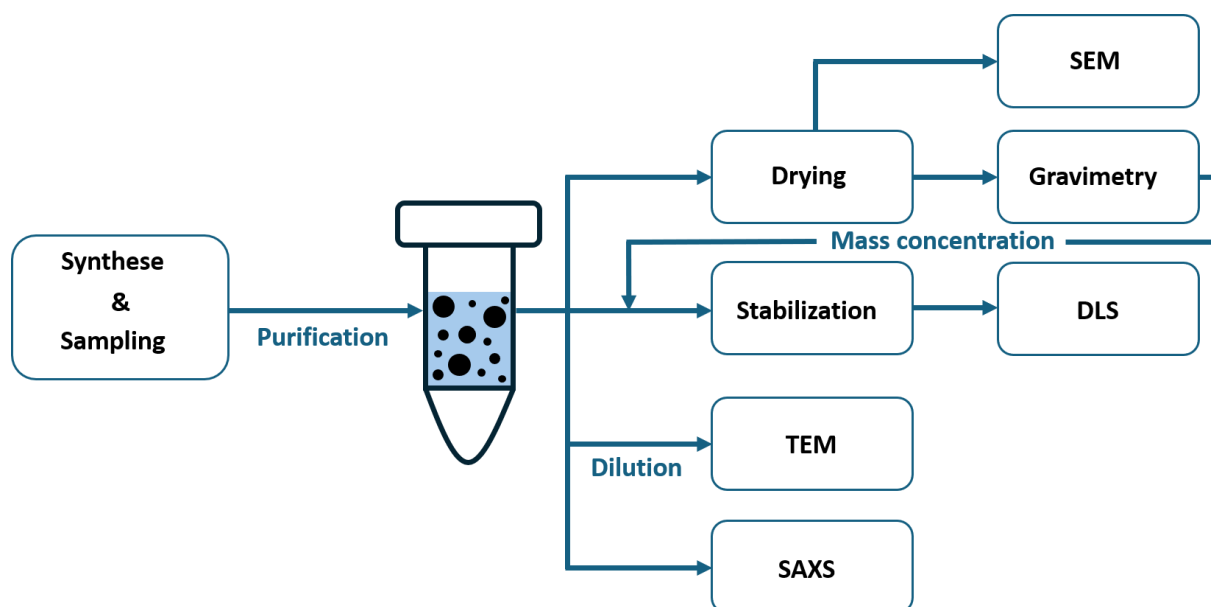


Figure 5. Workflow of sample preparation and measurement techniques.

2.4.1. Small angle X-ray scattering

SAXS experiments were performed using a Xeuss 2.0 Q-Xoom (Xenocs SA, Grenoble, France) instrument, equipped with a Genix3D Cu ULC (ultra-low divergence) micro focus source of Cu K α with an energy of 8.04 keV, a wavelength of 1.5406 Å, and a Pilatus3 R 300K detector (Dectris Ltd., Baden, Switzerland). The AZO nanoparticles dispersed in ethanol was injected into a flow cell, packed between two polyimide foils with a sample thickness of 0.5 mm. The 2D scattering patterns were obtained using sample-to-detector distances of 2500 mm and 500 mm, leading to accessible range of scattering vector (q) from 0.003 to 0.2 Å⁻¹. Utilizing Xenocs XSACT software, an azimuthal integration was applied to transform scattering patterns into 1D plots of the intensity $I(q)$ versus q with $q = 4\pi\sin(2\theta/2)/\lambda$, where 2θ is the scattering angle and λ is the wavelength of the Cu K α source. The measurement time was 600s. The plots for AZO particles were acquired by subtracting the intensity of pure ethanol. The hierarchical geometric mean diameters (d_{R_g}) of AZOs were quantified by applying Guinier laws to SAXS plots, calculated from $d_{R_g} = 2\sqrt{3}R_g$ where R_g is radius of gyration [40].

2.4.2. Stabilization and dynamic light scattering

The sequence of the stabilization and centrifugation process is modified according to the work of Zellmer and coworkers [40,41]. 3 ml sample (AZO in ethanol) was prepared in a 5 ml-glass. MEAA was employed as stabilizer to achieve steric stabilization. The amount of MEAA was determined based on the AZO concentration, ensuring that the mass concentration ratio of MEAA to non-stabilized dispersion equals 50 wt%. The adsorption of MEAA onto AZO surfaces was conducted by stirring at 1400 rpm via a magnetic stirrer for 24 hours at room temperature. The stabilized phase was acquired by centrifugation (Centrifuge 5430R, rotor FA454811, Eppendorf) with a g-force of 18930 at 20 °C. The subsequent DLS measurements focused on the stable phase.

2.4.3. Transmission Electron Microscopy and High-Angle Annular Dark-Field Imaging

The washed AZO samples in ethanol was strongly diluted to a concentration under 100 mg L⁻¹ and air-dried on a copper TEM grid at room temperature before investigating the crystallinity and morphology via TEM (Philips CM200). Additionally, HAADF-STEM combined with EDXS, was used to investigate chemical compositions of AZOs. The experiments were performed on the FEI Osiris ChemiSTEM microscope, equipped with a Super-X EDXS system comprising four silicon drift detectors. EDXS elemental maps of Zn (Zn-K α line), O (O-K α line) and Al (Al-K α line) were recorded and analyzed through the ESPRIT software (Bruker).

2.4.4. Scanning Electron Microscopy

The AZO powdered sample was applied to a carbon film. The subsequent examination of the sample was carried out in vacuum using the LEO 1530 microscope.

2.4.5. Drying and gravimetry

After sample purification, AZOs in ethanol were sequentially dispersed via a Vortex (IKA) and a Sonotrode Sonifier 450 (Branson Ultrasonics). Subsequently, 1 ml of the sample was pipetted into pre-weighed glass containers and dried in an oven (Memmert) for 24 hours at 80°C. Following complete evaporation of ethanol, AZO mass was quantified by calculating the mass difference of glass containers before and after drying. This process was repeated in triplicate, with three separate 1 ml-samples used to ensure accuracy and consistency of the results.

3. Results and discussion

3.1. Growth of AZO mesocrystals and doping level

As described in Section 2.1, once the secondary heating phase begins (from 50 °C to the target synthesis temperature), the reactions shown in Figure 2 initiate, leading to the formation of Zn-O-Zn monomers. According to crystallization theory, the high concentration of these monomers results in a high degree of supersaturation in BnNH_2 , which triggers nucleation and the formation of a large number of nuclei (the source of the primary particles). During the nucleation process, the monomer concentration decreases abruptly, preventing further nucleation [42]. SAXS analysis quantified the evolution of primary particle sizes (Figure 6b), expressed as geometric diameters (d_{R_g}), calculated from the formula $d_{R_g} = 2\sqrt{3}R_g$, where R_g is the radius of gyration determined by applying Guinier fits to the SAXS curves. The number concentration of primary crystals was derived from the d_{R_g} values and the AZO mass concentration, obtained via gravimetric analysis (Figure S7). Figure 6c presents that the number of primary AZO crystals stabilizes, demonstrating the early completion of nucleation within 13 minutes after raising temperature from 50 °C.

In parallel with the generation of primary nanocrystals through nucleation, nanoparticle assemblies evolved simultaneously, displaying a consistent wurtzite shape, characterized by a high degree of organization from primary particles with common crystallographic orientation (Figure 6b, e-f). This spontaneous self-organization of primary particles with a consistent crystallographic orientation, led to single crystalline with secondary particles, termed mesocrystals [43,44]. The hierarchical architecture of AZO mesocrystals was confirmed by SAXS (Figure 6a, sampling time: 13 minutes to 24 hours), characterized by two closely connected shoulders. The first shoulder at low q area ($0.01 - 0.03 \text{ \AA}^{-1}$) indicated the signal of mesocrystals while the second shoulder at high q range ($0.03 - 0.05 \text{ \AA}^{-1}$) correlated to the primary crystals. With increased sampling time, both shoulders shifted to the left, confirming growth of primary crystals (d_{R_g} : 10 nm \rightarrow 15 nm) and mesocrystals (d_{R_g} : 20 nm \rightarrow 30 nm). The exponential increase in size dominated within the first 50 minutes at 110 °C (Figure 6c).

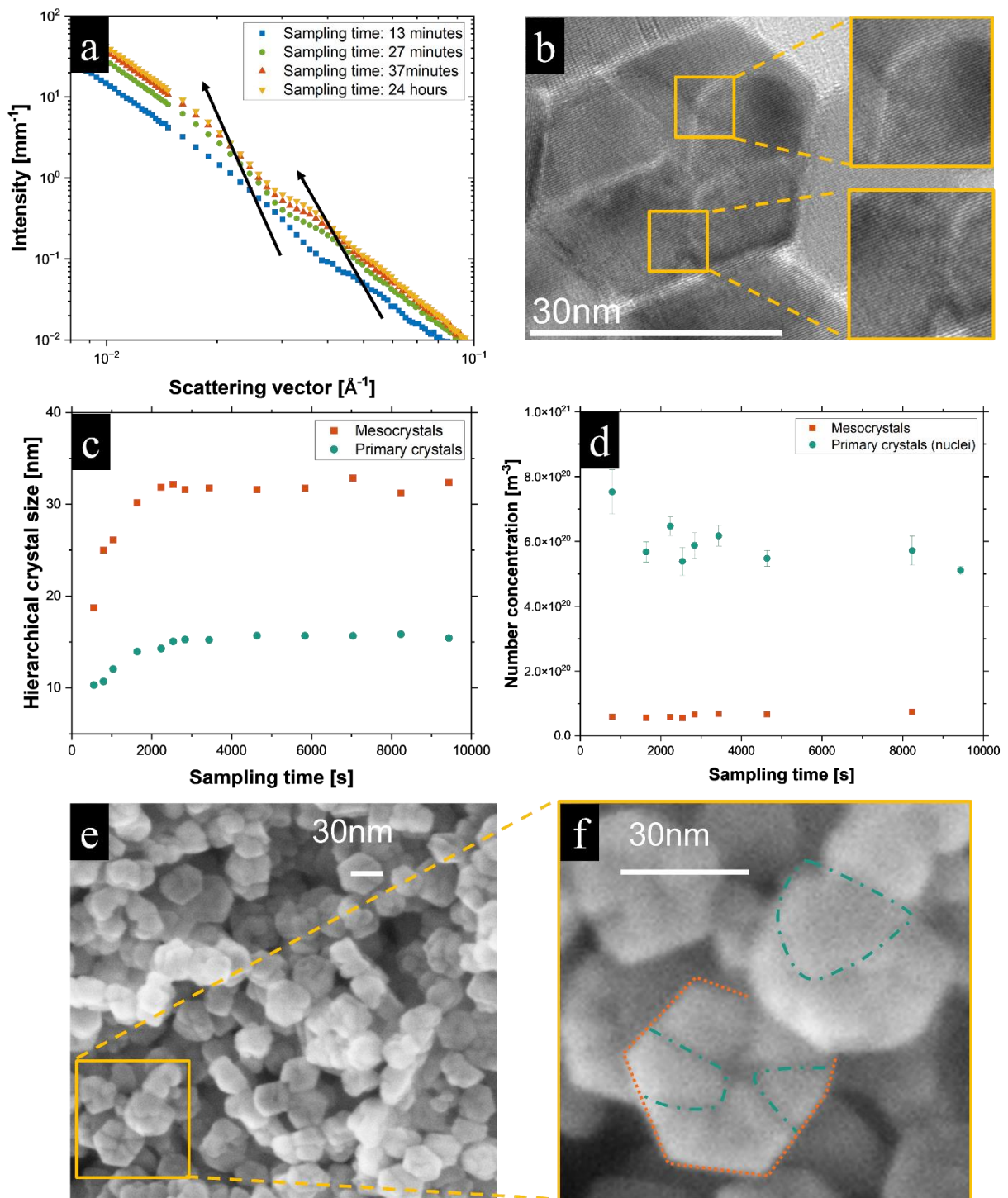


Figure 6. a) SAXS curves of representative AZO samples during synthesis; b) TEM image of AZO mesocrystals indicating organization with respect to the crystallographic orientation of adjacent primary particles. Arrows point to the bonds between primary crystals; c) evolution of AZO's hierarchical size, expressed as geometric diameters determined via Guinier fits on SAXS curves; d) time-resolved crystal number concentration, calculated based on d_{R_g} and AZO mass concentration; e) – f) SEM image showing a highlighted AZO mesocrystal consisting of highlighted primary crystals.

The observed oriented attachment process to form mesocrystals is proposed to be governed by strong interactions between numerous ZnO primary crystals in benzylamine, resulting from ongoing nucleation. Among the possible forces between primary particles in the liquid phase, dipole–dipole interactions have been proven capable of organizing primary particles through an oriented attachment process [45-48]. II–VI semiconductor nanocrystals, consisting of metals from group 2 or group 12 of the periodic table and a nonmetal from group 16, have been reported to exhibit considerable dipole moments within their hexagonal crystal structures [49-51]. Besides, benzylamine constitutes an environment of low dielectric constant ($\epsilon = 4.6$), which strongly enhances dipole–dipole interactions, facilitating the assembly into mesocrystals [52,53]. The tendency of amines to inhibit growth in the *l* direction (Figure 7f) at high concentrations is known for the ZnO synthesis in alkylamines [54]. Benzylamine's ability to stabilize the (001) crystal face (Figure 7f), and high anisotropic dipole moment of ZnO in a platelet shape, resulted in the mutual alignment of the non-stabilized faces, leading to the formation of mesocrystals in hexagonal platelet shapes (Figure 6b,e-f). After maintaining 110 °C for 24 hours, the reaction yield exceeded 90%. Despite a consistent crystallographic orientation within mesocrystals, pores (see Figure 7b) were clearly recognizable, primary particles were partially connected via crystalline bridges (Figure 6b) and voids between them persisted. The formation of these bridges between primary crystals is energetically favored as it helps eliminate high-energy surfaces. The persisting voids and pores can be attributed to the incomplete removal of benzylamine during synthesis [46].

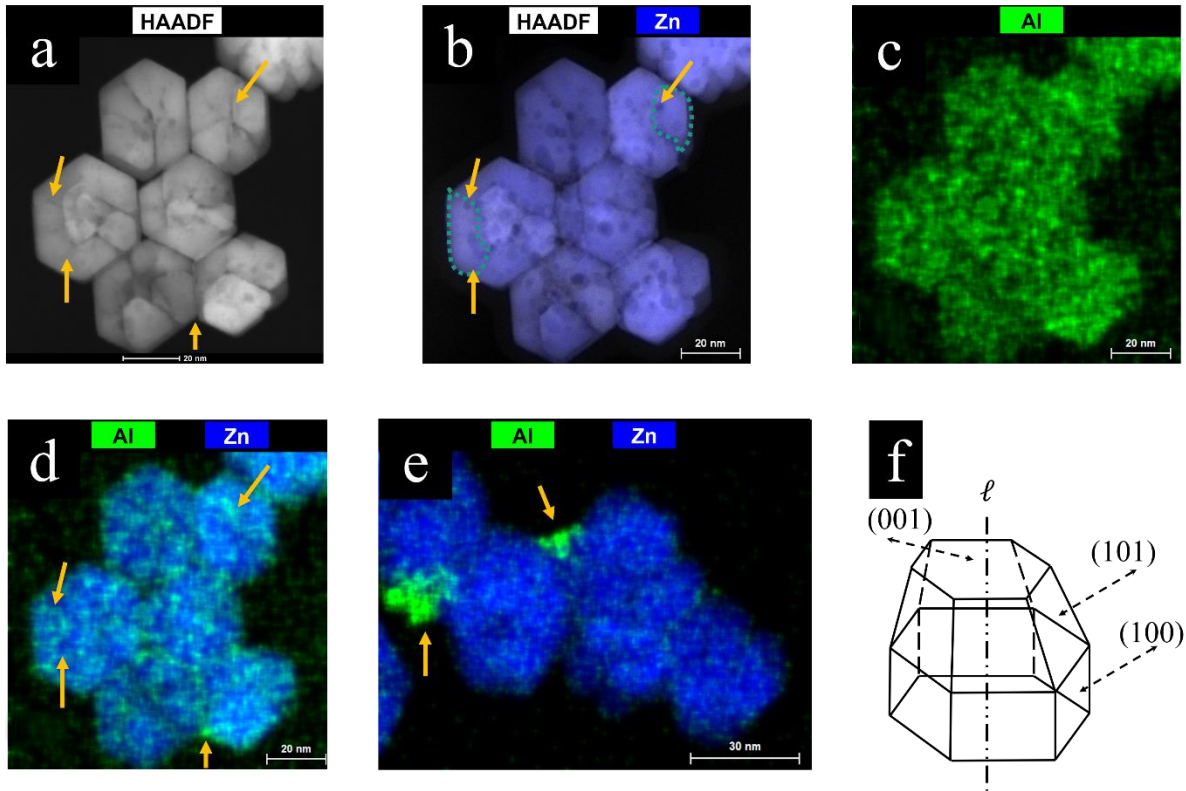


Figure 7. a) – e) HAADF-STEM images of AZO crystals. Arrows point to Al segregation at ZnO peripheries and intercrystallite boundaries. In b): primary crystals are highlighted and Al segregation on peripheries is indicated with arrows; f) idealized crystal faces of wurtzite ZnO.

Figure 7a–e shows the synthesized AZO particles obtained using HAADF-STEM combined with EDX analysis. When examining agglomerates of mesocrystals (Figure 7c), the Al composition determined by EDX (see Figure S10) was found to be 1.4 ± 0.4 at%, indicating that the Al content in the AZO particles was lower than the initial Al contents. This observation aligns with findings from other research groups [22], which suggest partial conversion of Al into ZnO during the process. Additionally, EDX mappings revealed the segregation of the Al dopant at the edges of primary ZnO particles (Figure 7b,d) and at mesocrystal boundaries (Figure 7e), consistent with previous reports [12]. The partial conversion of nominal Al and the inhomogeneous dopant distribution can be attributed to the high concentration of aluminum isopropoxide at the start of the process. Excess Al^{3+} ions that cannot be accommodated within the ZnO lattice tend to segregate at the surface and intercrystallite boundaries. This leads to stronger barrier to inter-particle electron conduction [55]. This phenomenon contributes to the high electrical resistivity observed in the manufactured AZO films, as measured by the four-point probe method. Despite the dopant segregation due to excess Al, a linear reduction in Al doping levels was reported by lowering the initial Al^{3+} concentration [22]. For future studies, it

is crucial to optimize the concentration of aluminum isopropoxide to enhance dopant distribution and conductivity.

3.2. Tailoring of AZO mesocrystals via control of heating durations

After analyzing the mechanisms of AZO mesocrystal formation and characterizing the hierarchical crystal growth, the impact of temperature profiles, specifically synthesis temperature and heating duration, on AZO size and morphology is investigated. This section focuses on evaluating the effects of heating durations. The key synthesis factors were maintained: 1) synthesis temperature of 110°C, 2) total reagent concentration of 25 g L⁻¹ (comprising 2.5 mol% Al(OiPr)₃ and 97.5 mol% Zn(acac)₂) in 250 ml BnNH₂. The primary variant was the heating duration to raise temperature from 50 °C to 110 °C.

In Equation 2 in Section 2.3, T_{50} and the temperature setpoint T_r represent the initial temperature (50 °C) and a constant synthesis temperature, respectively. The evolution of $T(t)$ adheres to an exponential function, gradually approaching the setpoint T_r asymptotically. In this section, T_r was set to 110 °C. Consequently, multiple temperature profiles were generated by manipulating τ_2 (Table 1), resulting in temperature profiles with different heating durations from 50 °C to 110 °C. The PI controller that regulates the actual reactor temperature, was calibrated to realize $T(t)$. By employing this model, the actual reactor temperature was controlled to mimic the behavior of the defined temperature trajectory $T(t)$ in a reproducible manner. Table 2 and Figure 8 summarize the key results for synthesis A – D with the same synthesis temperature of 110 °C, where heating durations increased from 7 to 19 minutes (see temperature profiles in Figure 8a). Further reducing the heating duration to less than 7 minutes is constrained by the thermal capacity of the heaters in use. The data in Table 2 correlate to the AZO products after being maintained at 110°C for 24 hours.

Table 2. Heating duration from 50 °C to reach 110 °C, mesocrystal size, Z-average, polydispersity index and the number of nuclei at a constant synthesis temperature of 110 °C.

Synthesis	Heating duration [min]	Size ^{a)} [nm]	\bar{Z} ^{b)} [nm]	PDI ^{b)}	PDI width ^{b)} [nm]	Number of nuclei ^{c)} [10 ²¹ m ⁻³]
A	7	24	18	0.08	5	1,70
B	9	23	20	0.04	4	1,76
C	12	23	21	0.06	5	1.74
D	19	36	45	0.05	10	N/A

^{a)} Geometric diameters of mesocrystals, calculated via Guinier-laws from SAXS data; ^{b)} DLS measurements focusing on the stabilized AZOs (growth after 24 hours), computed by Zetasizer. PDI width = $\bar{Z} \cdot \text{PDI}^{0.5}$ [57], and it quantifies the standard deviation of a normal distribution; ^{c)} number of nuclei, calculated based on geometric diameter and AZO mass.

The AZO crystals from synthesis A – D were investigated by SAXS. Figure 8b depicts the SAXS curves of the synthesis products where the synthesis temperature was maintained at 110 °C for more than 24 hours to achieve a reaction yield exceeding 90%. The resulting AZO crystals from synthesis A – C (heating durations: 7 – 12 minutes) exhibited similar SAXS pattern, characterized by two closely connected shoulders, indicating mesocrystals with common hierarchical structures and sizes. Additionally, the primary and mesocrystals showed similar exponential size evolution (Figure 8d), along with comparable evolution of the crystal number concentration (Figure 8e). Despite the similarity among the synthesis A – C, which delivered homogeneous AZO mesocrystals (Figure 8c), synthesis D that encountered the slowest heating process (19 minutes) to reach 110 °C, displayed an absence of similar characteristic shoulders, demonstrating a decline in the self-assembly quality. This observation was further confirmed by the SEM and TEM images. Figure 8f-h revealed new morphologies resulting from synthesis D, including a fraction of large AZO mesocrystals and the presence of small spherical crystals that lacked assembly into mesocrystals.

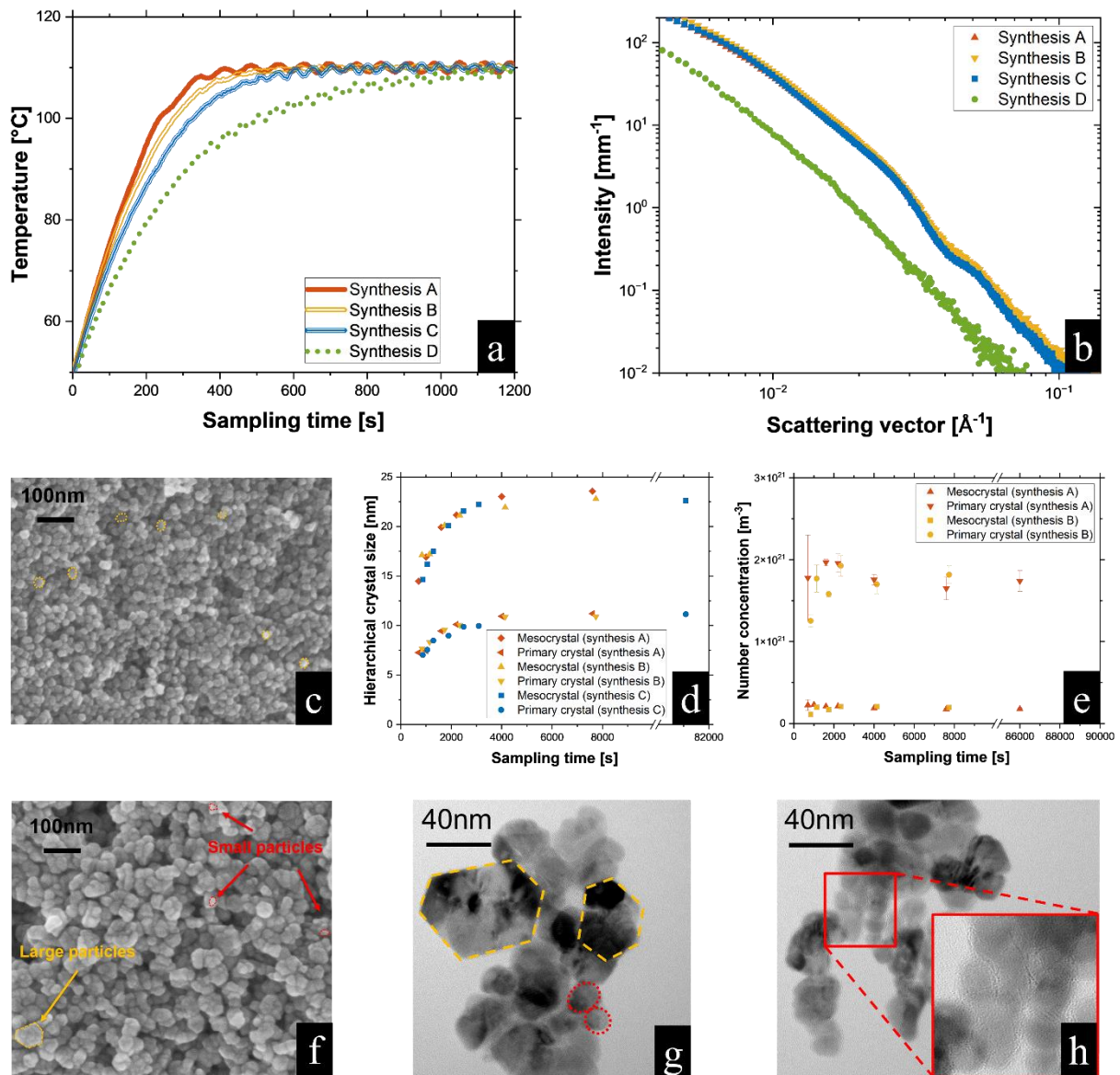


Figure 8. a) Temperature profiles showing the evolution of reactor temperatures for synthesis A – D; b) SAXS curves of AZO particles (growth after 24 hours in reactor); c) SEM images of homogeneous AZO mesocrystals from synthesis A; d) crystal growth; e) evolution of crystal number concentration; f) – h) SEM and TEM images of AZO crystals from synthesis D.

The observed differences between synthesis A – C and synthesis D indicates the importance of heating durations in sol-gel processes. The sensitivity of AZO morphologies to heating durations is proposed strongly related to the time span of nucleation. As demonstrated in previous sections, when heating the dispersion from 50 °C to 110 °C, the reaction kinetics to build up monomers initiated and progressed rapidly, resulting in a swift supersaturation of monomers within a short timeframe. According to the LaMer model, nucleation is fundamentally associated with the level of supersaturation, denoted as S . Nucleation initiates

only when the critical supersaturation threshold is initially attained, and ceases as the supersaturation decreases back to this critical value. The nucleation rate, as described by the classical theory of primary nucleation, is proportional to $\exp(-T^{-3}(\ln S)^{-2})$ [57,58]. This expression emphasizes the significance of temperature T on nucleation rates, due to its higher exponent and greater order of magnitude compared to $\ln S$. As depicted in Figure 8a, for the syntheses A, B and C, temperature increment from 50 °C to 110 °C occurred more rapidly (7, 9 and 12 minutes) compared to synthesis D (19 minutes), thereby triggering higher nucleation rates at an earlier stage, leading to a more pronounced reduction of monomer concentration to the critical S and fast completion of nucleation. Owing to their short burst of nucleation, the formed nuclei were overall uniform in size and morphology [59]. After further growth to primary crystals and the self-assembly into mesocrystals, the mesocrystals from synthesis A, B and C present uniform size (d_{R_g} up to 24 nm) and hexagonal morphology.

Considering the correlation between longer heating duration and extended nucleation time, it is rational to infer that synthesis D, which experienced the longest heating period (19 minutes), exhibited the largest time span of nucleation. As a result, it is more likely to allow nucleus formation with considerable difference in size. Since the critical nucleation radius is proportional to T^{-1} [60], initially at lower temperatures, larger nuclei were formed. Owing to a high degree of supersaturation and the successful benzylamine stabilization (described in Section 2.1) at the beginning of nucleation, the early-formed large nuclei underwent anisotropic growth and self-assembly to form hexagonal mesocrystals (Figure 8g). Conversely, in a later stage of nucleation, smaller nuclei were thermodynamically favored due to the increased temperature. However, the newly formed smaller particles encountered a reduced level of supersaturation, where isotropic and slow growth was preferred, leading to a fraction of small spherical particles (Figure 8h). Studies have demonstrated that particles grown slowly at low monomeric concentrations typically form spherical shapes, while high supersaturation levels lead to the development of anisotropic morphologies [61–64].

Besides the investigations utilizing SAXS and electron microscopy, the AZOs from synthesis A, B and D were stabilized by conducting a steric stabilization step with MEAA and subsequently measured by DLS (Figure 9). For the synthesis A and B, the measured Z-average in Figure 9a (\bar{Z} : 15 nm \rightarrow 20 nm) illustrated a similar size evolution to the SAXS-determined mesocrystal growth in Figure 9d (d_{R_g} : 15 nm \rightarrow 23 nm). This validated the successful stabilization of MEAA to the mesocrystal level. However, for synthesis D, the Z-average (\bar{Z} =

45 nm) was more than twice that of synthesis A and B ($\bar{Z} = 20$ nm). It points out the significant influence of the heating duration on varying crystal size. In addition to \bar{Z} , the measured PDI and PDI width (Table 2 and Figure 9b) are indicators for PSD-width. An overall decrease of PDI and PDI-width was observed for synthesis A, B and D, revealing the similar self-sharpening mechanisms regardless of the heating durations, owing to the diffusion-controlled growth. After the completion of nucleation, the precursor was continuously consumed through the diffusion-controlled growth on formed mesocrystal surfaces until the end of supersaturation. Smaller particles with larger surface-to-volume ratio exhibited a higher growth rate. Consequently, the particle size distribution became increasingly monodisperse with prolonged reaction time [65]. When the sampling time was approximately one hour, PDIs stabilized below 0.08, showcasing the high homogeneity of synthesis products and their narrow PSD. Taking the synthesis A as an example, the DLS-quantified PSD (18 ± 5 nm) was highly comparable with 22 ± 4 nm, acquired by counting 300 mesocrystals on SEM images. The growth of mesocrystals and the narrowing mechanism of PSD are clearly presented in Figure 9c. The PSD, combined with mass concentration, allowed for the determination of mesocrystals' number density distributions (Figure 9d and SI. 6) and parametrization of population balance models [38].

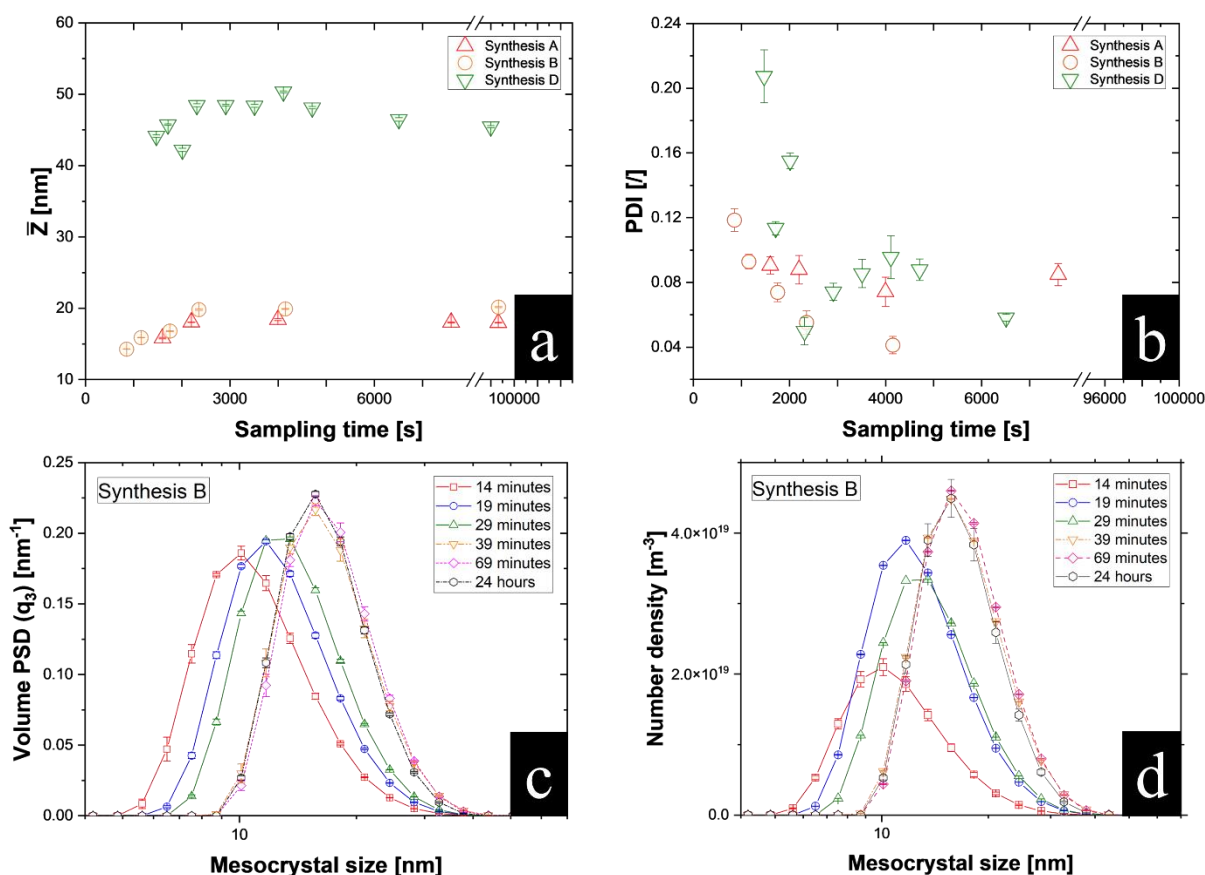


Figure 9. a) – b) time-resolved \bar{Z} and PDI; c) PSD evolution of mesocrystals; d) evolution of mesocrystals' number density distributions.

As has been demonstrated in this section, heating durations played a pivotal role in the sol-gel process for engineering particle size and morphology. The findings obtained highlight the importance of short heating durations in minimizing nucleation time span to obtain homogenous AZO nanoparticles. Specifically, maintaining heating durations under 12 minutes facilitated the production of homogeneous AZO mesocrystals (approximately 20 nm). However, prolonging the heating durations beyond a certain threshold led to considerable variations in the size and morphology of AZO particles, leading to the formation of larger hexagonal mesocrystals and a fraction of spherical particles. This phenomenon is likely related to variations in nucleus size and the sensitivity of particle growth mechanisms to the monomer's supersaturation level.

3.3. Tailoring of AZO mesocrystals via synthesis temperatures

After analyzing the effect of heating durations, the impact of synthesis temperatures on the AZO's hierarchical structure is examined in the final section. By adjusting the values of T_r in Equation 1, syntheses were conducted at varied synthesis temperatures: 105 °C (T105), 110 °C (T110), and 125 °C (T125). Lower temperatures were excluded due to reduced crystallinity associated with decreasing T_r . Following insights from Section 2.2, where minimizing heating duration was crucial for homogeneous particle formation, heating durations in this section were kept below 10 minutes by defining time constant τ_2 under 120 s (Table 1). Temperature profiles in Figure 10a presented similarities up to 100°C, facilitating a comparable evaluation. The key results are summarized in Table 3 and Figure 10.

Table 3. Heating duration from 50°C to reach individual synthesis temperature, mesocrystal size and aggregate size via SAXS characterization, Z-average and PDI of stabilized AZOs via DLS measurements, as well as the number of nuclei for synthesis T105 – T125 (AZO growth after 24 hours).

Synthesis	Heating duration [min]	Mesocrystal ^{a)} [nm]	Aggregate ^{a)} [nm]	\bar{Z} [nm]	PDI	Number of nuclei [10 ²⁰ m ⁻³]
T105	8	28	N/A	29	0.14	8,71
T110	7	24	N/A	18	0.08	17,3
T125	10	22	46	41	0.09	N/A

^{a)} geometric diameters of mesocrystals and aggregates, via Guinier-laws.

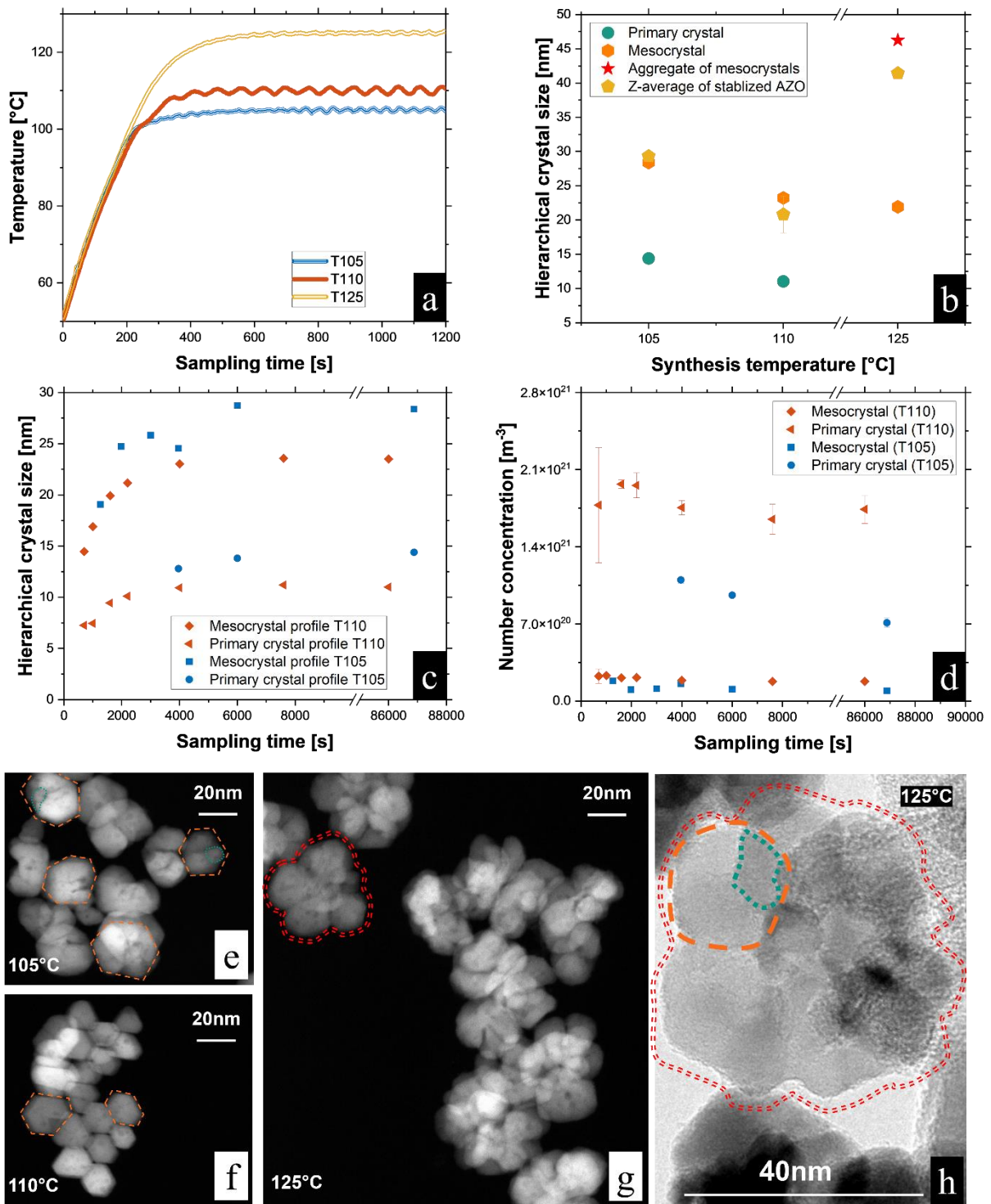


Figure 10. a) Temperature profiles employing different synthesis temperatures; b) hierarchical crystal size, characterized via SAXS and DLS, as a function of synthesis temperature; c) evolution of hierarchical size via SAXS; d) time-resolved crystal number concentration; e) – h) TEM images showing AZOs with increasing synthesis temperature. Three structural levels are highlighted, including primary crystals, mesocrystals and aggregates of mesocrystals.

TEM analysis (Figure 10e-h) displayed distinct differences in particle size at varying synthesis temperatures. Increasing the synthesis temperature from 105 °C to 110 °C led to smaller mesocrystals, confirmed by SAXS measurements (see Table 3 and Figure S2: d_{R_g} decreased from 28 nm to 24 nm). This size decline is attributed to the critical radius of nucleation, as discussed formerly. For T105, larger nuclei were favored, resulting in larger crystals (Figure 10c). Conversely for T110, smaller nuclei led to smaller mesocrystals, greater number of nuclei and crystals (Figure 10d). When increasing temperature to 125 °C, despite further reduction of mesocrystal size ($d_{R_g} = 22$ nm), the largest AZO particles were observed via TEM (Figure 10g-h). It is attributed to the aggregation of mesocrystals, which was not detected at low temperatures. Stabilization experiments confirmed irreversible assembly of mesocrystals into aggregates ($\bar{Z} = 41$ nm), aligning with SAXS ($d_{R_g} = 46$ nm).

Figure 10b summarizes the tunable hierarchical structures, including primary crystals, mesocrystals, and aggregates of mesocrystals, as a function of temperature. As the synthesis temperature increased from 105 °C to 125 °C, SAXS data revealed a reduction in mesocrystal size from 28 nm to 22 nm. Concurrently, the primary crystal size decreased from 15 nm to 11 nm between 105 °C and 110 °C. However, at 125 °C, a new mechanism emerged: the aggregation of mesocrystals, leading to the formation of the largest AZO aggregates ($d_{R_g} = 46$ nm). This aggregation diminished the scattering signal of the primary crystals, causing the failure of quantifying the primary particle size (Figure S3).

DLS analysis validated the development of hierarchical structures. Below a critical temperature, such as 105 °C and 110 °C, increasing the temperature facilitated the formation of smaller mesocrystals (\bar{Z} : 29 nm \rightarrow 18 nm). This formation of mesocrystals was explained in Section 2.1, resulting from the large dipole moments in benzylamine, which induced significant van der Waals forces between primary particles, leading to their irreversible coagulation into mesocrystals, in accordance with DLVO theory [64,65]. In contrast, the weaker attractive forces between mesocrystals, due to their larger hierarchical size, allowed for the separation of flocculated mesocrystals via stabilization with MEAA. However, when the temperature exceeded a critical threshold, e.g., at 125 °C, it triggered the irreversible aggregation of mesocrystals, and a higher structural level emerged [66]. The dominant van der Waals potential between mesocrystals prevented their redispersion. Besides, the increasing number of smaller primary crystals and mesocrystals, with a larger surface-to-volume ratio, weakened the stabilization effect of benzylamine on each crystal, especially the later-formed ones, resulting

in the failure of highly oriented attachment. The formation of large aggregates at 125 °C ($\bar{Z} = 46$ nm) likely stemmed from coagulation between mesocrystals and the direct integration of smaller particles onto mesocrystals. The findings highlight the influence of higher synthesis temperatures in decreasing size of existing structures and promoting their aggregation. Comparable effects were reported in the preparation of ZnO thin films using sol-gel methods. As the annealing temperature increased, larger ZnO particles and increased aggregation were observed [67-69].

4. Conclusion and perspective

In summary, an innovative temperature-controlled approach for nanoparticle tailoring in sol-gel processes has been developed, achieved through precisely imposing temperature profiles with specified synthesis temperatures and controlled heating durations. By implementing various temperature profiles that consider both temperatures and heating durations, hierarchical AZO structures were effectively modified in benzylamine. Variations in synthesis temperatures influenced the hierarchical size by affecting the number of nuclei and structural levels, with higher temperatures promoting aggregation and reducing the size of existing structures. For instance, controlling the synthesis temperature from 105 °C to 125 °C with heating durations under 10 minutes allowed for the adjustment of AZO size (\bar{Z} from 18 nm to 41 nm with a PDI below 0.14). Short heating durations (under 12 minutes) enabled the production of highly homogeneous AZO crystals, whereas longer heating time resulted in new particle morphologies. The temperature-controlled sol-gel process with short heating durations, ensures reproducible synthesis with consistent morphology. The resulting tunable, AZO nanocrystals with homogeneous morphology are well-suited for manufacturing thin films and studying the correlation between the optical and electrical properties of AZO functional materials and their particle characteristics. Based on the observed Al segregation on the ZnO peripheries and intercrystallite boundaries, it is crucial in future study to optimize the dopant distribution and enhance conductivity. The employed measurement techniques enabled quantification of hierarchical number concentration and nanoparticle properties, such as number density distributions of AZO mesocrystals, providing a feasible approach to parameterizing population balance models. This will facilitate integrating temperature control with process models for future nanoparticle tailoring research. Although this work centered on AZO particles, the methodology demonstrates the capability to characterize, predict and control particle characteristics through temperature adjustments. This highlights the potential of this

temperature-controlled method as an effective tailoring strategy for other materials, broadening the scope and applicability of this innovative approach.

Supporting information

Supporting Information is available from the ELSEVIER Online Library or from the author.

Acknowledgements

The authors acknowledge funding by the Deutsche Forschungsgemeinschaft (DFG, German Research Foundation) under the priority program “SPP 2364: Autonomous processes in particle technology” (NI 414/44-1 | ME 3231/10-1 – 504545992) and support from the KIT-Publication Fund of the Karlsruhe Institute of Technology. The authors thank H. Störmer and V. Zibat (Laboratory for Electron Microscopy, Karlsruhe Institute of Technology) for support with the electron microscopy, H. Su (Institute of Organic Chemistry, Karlsruhe Institute of Technology) for assistance with liquid chromatography.

References

- [1] Ellinger, C.R., Nelson, S.F., 2014. Selective Area Spatial Atomic Layer Deposition of ZnO, Al₂O₃, and Aluminum-Doped ZnO Using Poly(vinyl pyrrolidone). *Chem. Mater.* 26, 1514–1522. <https://doi.org/10.1021/cm402464z>
- [2] Meng, L., Chai, H., Yang, X., Lv, Z., Yang, T., 2019. Optically rough and physically flat TCO substrate formed by coating ZnO thin film on pyramid-patterned glass substrate. *Solar Energy Materials and Solar Cells* 191, 459–465. <https://doi.org/10.1016/j.solmat.2018.11.043>
- [3] Lee, S.J., Kim, S., Lim, D.C., Kim, D.H., Nahm, S., Han, S.H., 2019. Inverted bulk-heterojunction polymer solar cells using a sputter-deposited Al-doped ZnO electron transport layer. *Journal of Alloys and Compounds* 777, 717–722. <https://doi.org/10.1016/j.jallcom.2018.11.040>
- [4] Ellmer, K., Klein, A., Rech, B. (Ed.), 2008. *Transparent Conductive Zinc Oxide: Basics and Applications in Thin Film Solar Cells*, Volume 104. ed. Springer Science & Business Media, Berlin/Heidelberg.
- [5] Khan, Z.R., Alshammari, A.S., Bouzidi, M., Shkir, Mohd., Shukla, D.K., 2021. Improved optoelectronic performance of sol-gel derived ZnO nanostructured thin films. *Inorganic Chemistry Communications* 132, 108812. <https://doi.org/10.1016/j.inoche.2021.108812>
- [6] Clarke, B., Ghandi, K., 2023a. The Interplay of Growth Mechanism and Properties of ZnO Nanostructures for Different Applications. *Small* 19, 2302864. <https://doi.org/10.1002/sml.202302864>
- [7] Jing, Z., Zhan, J., 2008. Fabrication and Gas-Sensing Properties of Porous ZnO Nanoplates. *Advanced Materials* 20, 4547–4551. <https://doi.org/10.1002/adma.200800243>
- [8] Djurisić, A.B., Leung, Y.H., 2006. Optical properties of ZnO nanostructures. *Small* 2, 944–61. <https://doi.org/10.1002/sml.200600134>
- [9] Wang, M., Lee, K.E., Hahn, S.H., Kim, E.J., Kim, S., Chung, J.S., Shin, E.W., Park, C., 2007. Optical and photoluminescent properties of sol-gel Al-doped ZnO thin films. *Materials Letters* 61, 1118–1121. <https://doi.org/10.1016/j.matlet.2006.06.065>
- [10] Wang, R.-C., Liu, C.-P., Huang, J.-L., Chen, S.-J., 2006. Single-crystalline AlZnO nanowires/nanotubes synthesized at low temperature. *Applied Physics Letters* 88. <https://doi.org/10.1063/1.2161393>

- [11] Takaki, T., Kurosawa, K., Razavi, H., Sukenaga, S., Saito, N., Kaneko, K., Nakashima, K., Hiraaki, T., 2010. Electrolytic Synthesis of Al-Doped ZnO Nanopowders With Low Electrical Resistivity. *Journal of the American Ceramic Society* 93, 3088–3091. <https://doi.org/10.1111/j.1551-2916.2010.04048.x>
- [12] Nasr, B., Dasgupta, S., Wang, D., Mechau, N., Kruk, R., Hahn, H., 2010. Electrical resistivity of nanocrystalline Al-doped zinc oxide films as a function of Al content and the degree of its segregation at the grain boundaries. *Journal of Applied Physics* 108, 103721. <https://doi.org/10.1063/1.3511346>
- [13] Ammaih, Y., Lfakir, A., Hartiti, B., Ridah, A., Thevenin, P., Siadat, M., 2014. Structural, optical and electrical properties of ZnO:Al thin films for optoelectronic applications. *Opt Quant Electron* 46, 229–234. <https://doi.org/10.1007/s11082-013-9757-2>
- [14] Minami, T., 2008. Present status of transparent conducting oxide thin-film development for Indium-Tin-Oxide (ITO) substitutes. *Thin Solid Films* 516, 5822–5828. <https://doi.org/10.1016/j.tsf.2007.10.063>
- [15] Klingshirn, C., 2007. ZnO: material, physics and applications. *Chemphyschem* 8, 782–803. <https://doi.org/10.1002/cphc.200700002>
- [16] Luo, L., Rossell, M.D., Xie, D., Erni, R., Niederberger, M., 2013. Microwave-Assisted Nonaqueous Sol–Gel Synthesis: From Al:ZnO Nanoparticles to Transparent Conducting Films. *ACS Sustainable Chem. Eng.* 1, 152–160. <https://doi.org/10.1021/sc300073d>
- [17] Liu, R., Chen, Y., Ding, S., Li, Y., Tian, Y., 2019. Preparation of highly transparent conductive aluminum-doped zinc oxide thin films using a low-temperature aqueous solution process for thin-film solar cells applications. *Solar Energy Materials and Solar Cells* 203, 110161. <https://doi.org/10.1016/j.solmat.2019.110161>
- [18] Zhang, Z., Lu, M., Xu, H., Chin, W., 2007a. Shape-Controlled Synthesis of Zinc Oxide: A Simple Method for the Preparation of Metal Oxide Nanocrystals in Non-aqueous Medium. *Chemistry A European J* 13, 632–638. <https://doi.org/10.1002/chem.200600293>
- [19] Buha, J., Djerdj, I., Niederberger, M., 2007. Nonaqueous Synthesis of Nanocrystalline Indium Oxide and Zinc Oxide in the Oxygen-Free Solvent Acetonitrile. *Crystal Growth & Design* 7, 113–116. <https://doi.org/10.1021/cg060623+>
- [20] M., N., N., P. (Eds.), 2009. *Metal Oxide Nanoparticles in Organic Solvents: Synthesis, Formation, Assembly and Application*. Springer, London.

- [21] Ludi, B., Süess, M.J., Werner, I.A., Niederberger, M., 2012a. Mechanistic aspects of molecular formation and crystallization of zinc oxide nanoparticles in benzyl alcohol. *Nanoscale* 4, 1982–95. <https://doi.org/10.1039/c1nr11557j>
- [22] Niederberger, M., 2007. Nonaqueous Sol–Gel Routes to Metal Oxide Nanoparticles. *Acc. Chem. Res.* 40, 793–800. <https://doi.org/10.1021/ar600035e>
- [23] Chung, Y.T., Ba-Abbad, M.M., Mohammad, A.W., Hairom, N.H.H., Benamor, A., 2015. Synthesis of minimal-size ZnO nanoparticles through sol–gel method: Taguchi design optimisation. *Materials & Design* 87, 780–787. <https://doi.org/10.1016/j.matdes.2015.07.040>
- [24] Zellmer, S., Kockmann, A., Dosch, I., Temel, B., Garnweitner, G., 2015. Aluminum zinc oxide nanostructures with customized size and shape by non-aqueous synthesis. *CrystEngComm* 17, 6878–6883. <https://doi.org/10.1039/c5ce00629e>
- [25] Dutta, M., Mridha, S., Basak, D., 2008a. Effect of sol concentration on the properties of ZnO thin films prepared by sol–gel technique. *Applied Surface Science* 254, 2743–2747. <https://doi.org/10.1016/j.apsusc.2007.10.009>
- [26] Xu, L., Zheng, G., Miao, J., Xian, F., 2012a. Dependence of structural and optical properties of sol–gel derived ZnO thin films on sol concentration. *Applied Surface Science* 258, 7760–7765. <https://doi.org/10.1016/j.apsusc.2012.04.137>
- [27] Ungerer, J., Thurm, A.-K., Garnweitner, G., Nirschl, H., 2020. Formation of Aluminum-Doped Zinc Oxide Nanocrystals via the Benzylamine Route at Low Reaction Kinetics. *Chem Eng & Technol* 43, 797–803. <https://doi.org/10.1002/ceat.201900466>
- [28] Speaks, D.T., 2020. Effect of concentration, aging, and annealing on sol gel ZnO and Al-doped ZnO thin films. *Int J Mech Mater Eng* 15, 2. <https://doi.org/10.1186/s40712-019-0113-6>
- [29] Rajamanickam, S., Mohammad, S.M., Hassan, Z., 2020. Effect of zinc acetate dihydrate concentration on morphology of ZnO seed layer and ZnO nanorods grown by hydrothermal method. *Colloid and Interface Science Communications* 38, 100312. <https://doi.org/10.1016/j.colcom.2020.100312>
- [30] Arya, S., Mahajan, P., Mahajan, S., Khosla, A., Datt, R., Gupta, V., Young, S.-J., Oruganti, S.K., 2021a. Review—Influence of Processing Parameters to Control Morphology and Optical Properties of Sol-Gel Synthesized ZnO Nanoparticles. *ECS J. Solid State Sci. Technol.* 10, 023002. <https://doi.org/10.1149/2162-8777/abe095>

- [31] Zimmermann, M., Temel, B., Garnweitner, G., 2013. Parameter studies of the synthesis of titanium dioxide nanoparticles: Effect on particle formation and size. *Chemical Engineering and Processing: Process Intensification* 74, 83–89. <https://doi.org/10.1016/j.cep.2013.08.001>
- [32] Omri, K., Najeh, I., Dhahri, R., El Ghouli, J., El Mir, L., 2014. Effects of temperature on the optical and electrical properties of ZnO nanoparticles synthesized by sol–gel method. *Microelectronic Engineering* 128, 53–58. <https://doi.org/10.1016/j.mee.2014.05.029>
- [33] Pinna, N., Garnweitner, G., Antonietti, M., Niederberger, M., 2005. A general nonaqueous route to binary metal oxide nanocrystals involving a C-C bond cleavage. *J Am Chem Soc* 127, 5608–12. <https://doi.org/10.1021/ja042323r>
- [34] Oskam, G., 2006. Metal oxide nanoparticles: synthesis, characterization and application. *J Sol-Gel Sci Technol* 37, 161–164. <https://doi.org/10.1007/s10971-005-6621-2>
- [35] Xia, Y., Xiong, Y., Lim, B., Skrabalak, S.E., 2009. Formkontrolle bei der Synthese von Metallnanokristallen: einfache Chemie, komplexe Physik? *Angewandte Chemie* 121, 62–108. <https://doi.org/10.1002/ange.200802248>
- [36] Berger, C., Hoffmann, U., Braunreuther, S., Reinhart, G., 2018. Modeling, simulation, and control of production resource with a control theoretic approach. *Procedia CIRP* 67, 122–127. <https://doi.org/10.1016/j.procir.2017.12.187>
- [37] U. Heinz, 2008. *Regelungstechnik I: Klassische Verfahren zur Analyse und Synthese linearer kontinuierlicher Regelsysteme, Fuzzy-Regelsysteme*, Springer-Verlag, Wiesbaden.
- [38] Jiokeng Dongmo, M.K., Guohui, Y., Nirschl, H., Meurer, T., 2024. Moving Horizon Estimator Design for a Nanoparticle Synthesis Batch Process. *IFAC-PapersOnLine* 58, 342–347. <https://doi.org/10.1016/j.ifacol.2024.08.360>
- [39] Ungerer, J., Thurm, A.-K., Meier, M., Klinge, M., Garnweitner, G., Nirschl, H., 2019. Development of a growth model for aluminum-doped zinc oxide nanocrystal synthesis via the benzylamine route. *J Nanopart Res* 21, 106. <https://doi.org/10.1007/s11051-019-4547-9>
- [40] Ungerer, J., Thurm, A.-K., Garnweitner, G., Nirschl, H., 2020. Evaluation of the Dispersion Stability of AZO Mesocrystals for Their Processing into Functional Thin Films Using Small Angle X-ray Scattering. *Crystals* 10, 374. <https://doi.org/10.3390/cryst10050374>

- [41] Kind, M., Peukert, W., Rehage, H., Schuchmann, H.P. (Eds.), 2015. Colloid Process Engineering. Springer International Publishing, Cham. <https://doi.org/10.1007/978-3-319-15129-8>
- [42] Xia, Y., Xiong, Y., Lim, B., Skrabalak, S.E., 2009. Formkontrolle bei der Synthese von Metallnanokristallen: einfache Chemie, komplexe Physik? *Angewandte Chemie* 121, 62–108. <https://doi.org/10.1002/ange.200802248>
- [43] Song, R., Cölfen, H., 2010. Mesocrystals—Ordered Nanoparticle Superstructures. *Advanced Materials* 22, 1301–1330. <https://doi.org/10.1002/adma.200901365>
- [44] Zhou, L., O'Brien, P., 2008b. Mesocrystals: a new class of solid materials. *Small* 4, 1566–74. <https://doi.org/10.1002/sml.200800520>
- [45] Olliges-Stadler, I., Rossell, M.D., Süess, M.J., Ludi, B., Bunk, O., Pedersen, J.S., Birkedal, H., Niederberger, M., 2013. A comprehensive study of the crystallization mechanism involved in the nonaqueous formation of tungstite. *Nanoscale* 5, 8517. <https://doi.org/10.1039/c3nr02020g>
- [46] Penn, R.L., Soltis, J.A., 2014. Characterizing crystal growth by oriented aggregation. *CrystEngComm* 16, 1409. <https://doi.org/10.1039/c3ce41773e>
- [47] Ludi, B., Süess, M.J., Werner, I.A., Niederberger, M., 2012. Mechanistic aspects of molecular formation and crystallization of zinc oxide nanoparticles in benzyl alcohol. *Nanoscale* 4, 1982–95. <https://doi.org/10.1039/c1nr11557j>
- [48] Jia, B., Gao, L., 2008. Growth of Well-Defined Cubic Hematite Single Crystals: Oriented Aggregation and Ostwald Ripening. *Crystal Growth & Design* 8, 1372–1376. <https://doi.org/10.1021/cg070300t>
- [49] Shanbhag, S., Kotov, N.A., 2006. On the Origin of a Permanent Dipole Moment in Nanocrystals with a Cubic Crystal Lattice: Effects of Truncation, Stabilizers, and Medium for CdS Tetrahedral Homologues. *J. Phys. Chem. B* 110, 12211–12217. <https://doi.org/10.1021/jp0611119>
- [50] Lu, W., Gao, P., Jian, W.B., Wang, Z.L., Fang, J., 2004. Perfect Orientation Ordered in-Situ One-Dimensional Self-Assembly of Mn-Doped PbSe Nanocrystals. *J. Am. Chem. Soc.* 126, 14816–14821. <https://doi.org/10.1021/ja046769j>
- [51] Tang, Z., Zhang, Z., Wang, Y., Glotzer, S.C., Kotov, N.A., 2006. Self-Assembly of CdTe Nanocrystals into Free-Floating Sheets. *Science* 314, 274–278. <https://doi.org/10.1126/science.1128045>
- [52] Bergström, L., 1997. Hamaker constants of inorganic materials. *Advances in Colloid and Interface Science* 70, 125–169. [https://doi.org/10.1016/S0001-8686\(97\)00003-1](https://doi.org/10.1016/S0001-8686(97)00003-1)

- [53] Arthur, A.M., Edgar, R.S., 1951. Table of Dielectric Constants of Pure Liquids.
- [54] Zhang, Z., Lu, M., Xu, H., Chin, W., 2007. Shape-Controlled Synthesis of Zinc Oxide: A Simple Method for the Preparation of Metal Oxide Nanocrystals in Non-aqueous Medium. *Chemistry A European J* 13, 632–638.
<https://doi.org/10.1002/chem.200600293>
- [55] Lin, J.-P., Wu, J.-M., 2008. The effect of annealing processes on electronic properties of sol-gel derived Al-doped ZnO films. *Applied Physics Letters* 92, 134103.
<https://doi.org/10.1063/1.2905279>
- [56] Raval, N., Maheshwari, R., Kalyane, D., Youngren-Ortiz, S.R., Chougule, M.B., Tekade, R.K., 2019. Importance of Physicochemical Characterization of Nanoparticles in Pharmaceutical Product Development, in: *Basic Fundamentals of Drug Delivery*. Elsevier, pp. 369–400. <https://doi.org/10.1016/B978-0-12-817909-3.00010-8>
- [57] LaMer, V.K., Dinegar, R.H., 1950. Theory, Production and Mechanism of Formation of Monodispersed Hydrosols. *J. Am. Chem. Soc.* 72, 4847–4854.
<https://doi.org/10.1021/ja01167a001>
- [58] Coulson, J.M., Richardson, J.F., 2010. *Chemical engineering. 2: Particle technology and separation processes*, 5. ed., repr. ed. Butterworth Heinemann, Amsterdam.
- [59] Sugimoto, T., 1987. Preparation of monodispersed colloidal particles. *Advances in Colloid and Interface Science* 28, 65–108. [https://doi.org/10.1016/0001-8686\(87\)80009-X](https://doi.org/10.1016/0001-8686(87)80009-X)
- [60] Thanh, N.T.K., Maclean, N., Mahiddine, S., 2014. Mechanisms of Nucleation and Growth of Nanoparticles in Solution. *Chem. Rev.* 114, 7610–7630.
<https://doi.org/10.1021/cr400544s>
- [61] Peng, X., 2003. Mechanisms for the Shape-Control and Shape-Evolution of Colloidal Semiconductor Nanocrystals. *Advanced Materials* 15, 459–463.
<https://doi.org/10.1002/adma.200390107>
- [62] Peng, Z.A., Peng, X., 2002. Nearly Monodisperse and Shape-Controlled CdSe Nanocrystals via Alternative Routes: Nucleation and Growth. *J. Am. Chem. Soc.* 124, 3343–3353. <https://doi.org/10.1021/ja0173167>
- [63] Peng, X., Manna, L., Yang, W., Wickham, J., Scher, E., Kadavanich, A., Alivisatos, A.P., 2000. Shape control of CdSe nanocrystals. *Nature* 404, 59–61.
<https://doi.org/10.1038/35003535>

- [64] Manna, L., Scher, E.C., Alivisatos, A.P., 2000. Synthesis of Soluble and Processable Rod-, Arrow-, Teardrop-, and Tetrapod-Shaped CdSe Nanocrystals. *J. Am. Chem. Soc.* 122, 12700–12706. <https://doi.org/10.1021/ja003055+>
- [65] Ring, T.A., 1996. *Fundamentals of ceramic powder processing and synthesis.* Academic press, San Diego New York Boston.
- [66] Garnweitner, G., Grote, C., 2010a. Die nicht-wässrige Sol-Gel-Synthese – eine Alternative für die Herstellung hochqualitativer Metalloxid- Nanopartikel. *Chemie Ingenieur Technik* 82, 615–622. <https://doi.org/10.1002/cite.200900151>
- [67] Lv, J., Gong, W., Huang, K., Zhu, J., Meng, F., Song, X., Sun, Z., 2011. Effect of annealing temperature on photocatalytic activity of ZnO thin films prepared by sol–gel method. *Superlattices and Microstructures* 50, 98–106. <https://doi.org/10.1016/j.spmi.2011.05.003>
- [68] Kayani, Z.N., Saleemi, F., Batool, I., 2015. Effect of calcination temperature on the properties of ZnO nanoparticles. *Appl. Phys. A* 119, 713–720. <https://doi.org/10.1007/s00339-015-9019-1>
- [69] Ismail, A.M., Menazea, A.A., Kabary, H.A., El-Sherbiny, A.E., Samy, A., 2019. The influence of calcination temperature on structural and antimicrobial characteristics of zinc oxide nanoparticles synthesized by Sol–Gel method. *Journal of Molecular Structure* 1196, 332–337. <https://doi.org/10.1016/j.molstruc.2019.06.084>

Table of contents

Herein, we present a novel temperature-controlled strategy aimed at customizing the hierarchical structures of nanocrystals in a sol-gel process. By implementing different temperature profiles and performing hierarchical characterization, the correlation between temperature profiles and particle properties is thoroughly investigated. Significant modification to nanoparticles is achieved while maintaining the same precursor concentration with minor variations in synthesis temperatures.

Guohui Yang, Marcel Kévin Jiokeng Dongmo, Simon Buchheiser, Thomas Meurer, Hermann Nirschl*

Temperature-Driven Strategy for Engineering of Al-Doped ZnO Mesocrystals' Hierarchical Architecture

